Numerical experiments on the performance of the RBF meshfree Galerkin Methods for solid mechanics

Abderrachid Hamrani, Eric Monteiro, Idir Belaidi, Philippe Lorong

Abstract—In this work the advances in meshfree methods, particularly the Radial Basis Function based meshfree Galerkin Methods, are presented with the purpose of analyzing the performance of their meshless approximations and integration techniques. The Radial Point Interpolation Method (RPIM) is studied based on the global Galerkin weak form performed using classical Gaussian integration and the stabilized conforming nodal integration scheme. The numerical performance of this category of methods is tested on their behavior on two elastic problems with regular node grids, and two other with distorted irregular grids. All RPIM methods perform very well in term of elastic computation, the Smoothed Radial Point Interpolation Method (SRPIM) shows a higher accuracy, especially in a situation of distorted node schemes. *Keywords*—adial Basis Function Radial Point Interpolation Method Galerkin weak form Nodal Integrationadial Basis Function Radial Point Interpolation Method Galerkin weak form Nodal IntegrationR

Keywords—Radial Basis Function, Galerkin weak form, Nodal Integration.

I. Introduction

ONE of the most important progress in the field of the numerical simulation was the development of the finite element method (FEM). In this method, a continuum solid defined by an infinity of material points is divided into finite elements which are connected between them by a kind of "grid". The finite element method (FEM) proved to be effective and robust in several engineering fields because of its capacity to deal with complex geometries. However, it remains that this method suffers from some limitations related to the use of meshes, especially when severe element distortions take place under large deformation processes where the accuracy in FEM results are considerably lost [1]. To surmount these problems, numerical methods known usually as "meshless" or "meshfree" methods were proposed, in these methods the problem domain is represented by a set of scattered nodes, without the need of any, a priori, information on the relationship between them. The development of some of the meshless methods goes back to more than seventy years, with the appearance of collocation methods [3] [4] [5]. After that, the first well known meshless method: the Smoothed Particle Hydrodynamics (SPH) [6], was originally created for the simulation of astrophysical phenomena by Lucy [7], and from the early 1990s, numerous methods have been proposed; for instance the diffuse element method (DEM) [8], the reproducing kernel particle method (RKPM) [9] [10],the element free Galerkin (EFG) method [11], the point interpolation methods [12], the meshless local Petrov-Galerkin method (MLPG) [13]. These methods use "Meshless" shape functions to represent the field variables, since these shape functions are mathematically constructed by using only a set of nodes without requiring a mesh.

The Moving least square (MLS) interpolation was one of the first shape functions used by Belytschko et al. [14] for the development of the element free Galerkin (EFG) method, and because of the limitations which suffered this method, in particular, the complexity of the calculations of MLS shape functions and their partial derivatives, besides the difficulty to imposing boundary conditions [15], Liu and Gu [16], [17] proposed a new family of meshless shape functions, that they called "Point Interpolation Methods". Among these methods, the radial point interpolation method (RPIM) is preferred because the use of radial basis function avoids us falling in the singularity problem of the conventional PIM [18] [45], and shape functions resulting from RBF are stable and hence flexible for arbitrary and irregular nodal configurations. For the achievement of a numerical simulation for mechanics problems we need in combination with shape function a formulation procedure based on strong or weak-forms derived directly from the physical principles. In general, we use weak-form formulations to construct discretized system equations, and the most widely used approache is the Galerkin weak-forms.

For the requirement of a weaker consistency on the approximate function, weak forms need an integral operation performed numerically by the use of two major techniques, the classical Gauss integration and the stabilized conforming nodal integration (SCNI) proposed by Beissel and Belytschko [19] and after by Chen et al. [20] [21].

In the present work, our objectif is to study the RBF meshfree Galerkin Methods through their performances in term of : interpolations (RPIM shape function) and their numerical integration techniques (classical Gauss integration and the stabilized conforming nodal integration).

II. Construction of RPIM shape functions

The interpolation employed for the construction of the RPIM shape functions augmented with polynomials can be

A. Hamrani and I. Belaidi are with Equipe de recherche Mécanique et Ingénierie des Systèmes et Procédés, LEMI. University of M'Hamed Bougara de Boumerdes, 35000, Algérie. (e-mail : hamrani.abderrachid@gmail.com, idir.belaidi@umbb.dz)

E. Monteiro and P. Lorong are with PIMM, Arts et Métiers ParisTech, CNRS, 151 bd de l'Hôpital, 75013 Paris, France. (email : Eric.MONTEIRO@ensam.eu, Philippe.LORONG@ensam.eu)

written as [45]:

$$u(\mathbf{x}) = \sum_{i=1}^{n} r_i(\mathbf{x})\ a_i + \sum_{j=1}^{m} p_j(\mathbf{x})\ b_j = \mathbf{r}^T(\mathbf{x})\,\mathbf{a} + \mathbf{p}^T(\mathbf{x})\,\mathbf{b} \quad (1)$$

Where $r_i(\mathbf{x})$ is a radial basis function (FRB), $p_j(\mathbf{x})$ is a basis function of monomials $[x, y]$ (in 2D problems). Coefficients a_i and b_i are the corresponding constants yet to be determined, n is the number of RBFs, m is the number of polynomial basis functions.

To find out coefficients a_i et b_i, we have to satisfy equation (1) at the n nodes in the local support domain of the point of interest at $\mathbf{x}$, this leads to n linear equations, then the matrix form of these equations can be written as :

$$\mathbf{u} = \mathbf{R}_0\,\mathbf{a} + \mathbf{P}_m\,\mathbf{b} \quad (2)$$

where :

$$\mathbf{u} = \begin{Bmatrix} u_1 & u_2 & u_3 & \cdots & u_n \end{Bmatrix}^T \quad (3)$$

the FBR matrix :

$$\mathbf{R}_0 = \begin{bmatrix} r_1(d_1) & r_2(d_1) & \cdots & r_n(d_1) \\ r_1(d_2) & r_2(d_2) & \cdots & r_n(d_2) \\ \cdots & \cdots & \cdots & \cdots \\ r_1(d_n) & r_2(d_n) & \cdots & r_n(d_n) \end{bmatrix}_{(n \times n)} \quad (4)$$

Where d_i in $r_i(d_k)$ is defined as :

$$d_k = \sqrt{(x_k - x_i)^2 + (y_k - y_i)^2} \quad (5)$$

and the Polynomial basis functions matrix:

$$\mathbf{P}_m = \begin{bmatrix} 1 & x_1 & y_1 & \cdots & p_m(x_1) \\ 1 & x_2 & y_2 & \cdots & p_m(x_2) \\ \vdots & \vdots & \vdots & \ddots & \vdots \\ 1 & x_n & y_n & \cdots & p_m(x_n) \end{bmatrix} \quad (6)$$

in this case, there are $n + m$ variables in Eq.2, so an other m equations should be required. Golberg et al.[22] added the additional m equations by using the following constraint conditions :

$$\mathbf{P}_m^T \mathbf{a} = \sum_{i=1}^{n} p_j(\mathbf{x}_i)\, a_i = 0, \qquad j = 1,\ 2,\ \ldots,\ m \quad (7)$$

the vector that collect coefficients for RBFs is :

$$\mathbf{a}^T = \begin{Bmatrix} a_1 & a_2 & \cdots & a_n \end{Bmatrix} \quad (8)$$

the vector that collect coefficients for Polynomial basis functions is :

$$\mathbf{b}^T = \begin{Bmatrix} b_1 & b_2 & \cdots & b_m \end{Bmatrix} \quad (9)$$

the equation (2) can be written in the following form:

$$\tilde{\boldsymbol{u}} = \begin{bmatrix} \mathbf{u} \\ 0 \end{bmatrix} = \underbrace{\begin{bmatrix} \mathbf{R}_0 & \mathbf{P}_m \\ \mathbf{P}_m^T & 0 \end{bmatrix}}_{\mathbf{G}} \begin{Bmatrix} \mathbf{a} \\ \mathbf{b} \end{Bmatrix} = \mathbf{G}\,\mathbf{a}_0 \quad (10)$$

$$\mathbf{a}_0^T = \begin{Bmatrix} a_1 & a_2 & \cdots & a_n & b_1 & b_2 & \cdots & b_m \end{Bmatrix} \quad (11)$$

$$\tilde{\boldsymbol{u}} = \begin{Bmatrix} u_1 & u_2 & \cdots & u_n & 0 & 0 & \cdots & 0 \end{Bmatrix} \quad (12)$$

Since the matrix $\mathbf{R}_0$ is symmetric, the matrix $\mathbf{G}$ will also be symmetric, than by solving equation (10), we obtain :

$$\mathbf{a}_0 = \begin{Bmatrix} \mathbf{a} \\ \mathbf{b} \end{Bmatrix} = \mathbf{G}^{-1}\,\tilde{\boldsymbol{u}} \quad (13)$$

The RPIM shape function is finally expressed as

$$\mathbf{u}(\mathbf{x}) = \begin{Bmatrix} \mathbf{r}^T(\mathbf{x}) & \mathbf{p}^T(\mathbf{x}) \end{Bmatrix} \begin{Bmatrix} \mathbf{a} \\ \mathbf{b} \end{Bmatrix} \quad (14)$$

$$u(\mathbf{x}) = \begin{Bmatrix} \mathbf{r}^T(\mathbf{x}) & \mathbf{p}^T(\mathbf{x}) \end{Bmatrix} \mathbf{G}^{-1}\tilde{\boldsymbol{u}} = \tilde{\boldsymbol{\phi}}^T(\mathbf{x})\,\tilde{\boldsymbol{u}} \quad (15)$$

$$\tilde{\boldsymbol{\phi}}^T(\mathbf{x}) = \begin{Bmatrix} \mathbf{r}^T(\mathbf{x}) & \mathbf{p}^T(\mathbf{x}) \end{Bmatrix} \mathbf{G}^{-1} \quad (16)$$

$$\tilde{\boldsymbol{\phi}}^T(\mathbf{x}) = \begin{Bmatrix} \phi_1(\mathbf{x}) & \phi_2(\mathbf{x}) & \cdots & \phi_n(\mathbf{x}) & \phi_{n+m}(\mathbf{x}) \end{Bmatrix} \quad (17)$$

Where the RPIM shape functions corresponding to the nodal displacements are given by

$$\boldsymbol{\phi}^T(\mathbf{x}) = \begin{Bmatrix} \phi_1(\mathbf{x}) & \phi_2(\mathbf{x}) & \cdots & \phi_n(\mathbf{x}) \end{Bmatrix} \quad (18)$$

It can be seen that the resultant RPIM shape function has the delta Kronecker property and partition of unity, and due to the addition of polynomial basis, they also fulfill the reproducing properties. In this work, different radial basis functions augmented with the linear polynomial basis are used to construct the present RPIM shape function, the choice of the shape parameters in the RBFs are studied.

III. Galerkin weak form of 2-D solid mechanics

A 2-D problem of solid mechanics defined in the domain Ω bounded by Γ can be described by the following equilibrium equation :

$$\nabla\cdot\boldsymbol{\sigma} + \mathbf{F} = 0 \quad in\ \Omega \quad (19)$$

where $\boldsymbol{\sigma}$ is the Cauchy stress tensor and $\mathbf{F}$ the body forces vector. The boundary conditions for the equilibrium equations are :

$$\boldsymbol{\sigma}\,\mathbf{n} = \bar{\mathbf{t}} \quad on\ the\ natural\ boundary\ \Gamma_t \quad (20)$$

$$\mathbf{u} = \bar{\mathbf{u}} \quad on\ the\ essential\ boundary\ \Gamma_u \quad (21)$$

where $\bar{\mathbf{u}}$ is a prescribed displacement on boundary Γ_u, $\bar{\mathbf{t}}$ is a prescribed traction on the boundary Γ_t and $\mathbf{n}$ is the outward normal on the boundary.

The well-known Galerkin weak form is given by :

$$\int_{\Omega} \delta\left(\nabla\mathbf{u}^T\right)\cdot\boldsymbol{\sigma}\,d\Omega - \int_{\Omega} \delta\mathbf{u}^T\cdot\mathbf{F}\,d\Omega - \int_{\Gamma_t} \delta\mathbf{u}^T\cdot\bar{\boldsymbol{t}}\,d\Gamma = 0 \quad (22)$$

Discretization of Eq.(22) with interpolation function Eq.(15) yields

$$\mathbf{K}\,\mathbf{u} = \mathbf{f} \quad (23)$$

where

$$\begin{aligned}\mathbf{K}_{ij} &= \int_{\Omega} \mathbf{B}_i^T\, \mathbf{C}\mathbf{B}_j\, d\Omega,\ and\ \mathbf{f}_i \\ &= \int_{\Omega} \mathbf{\Phi}_i^T\, \boldsymbol{F}\, d\Omega + \int_{\Gamma_t} \mathbf{\Phi}_i^T\, \bar{\boldsymbol{t}}\, d\Gamma\end{aligned} \tag{24}$$

where $\mathbf{C}$ is the matrix of elastic constants and $\mathbf{B}_i$ is the strain matrix.

The integrals involved in Eq.(24) are usually evaluated numerically through the well known Gauss integration scheme as is commonly used in finite elements. In this study, a second scheme is also used : the stabilized conform-ingnodal integration scheme (SCNI). Both schemes are shortly explained below.

IV. Integration techniques

A. Gauss integration

In order to evaluate integrals over the global problem domain Ω and the global traction boundary Γ_t, the problem domain is discretized into a set of background cells. Hence, a global integration can be expressed as :

$$\int_{\Omega} \mathbf{G}\, d\Omega\ = \sum_{k=1}^{n_c} \int_{\Omega_k} \mathbf{G}\, d\Omega = \sum_{k=1}^{n_c} \sum_{i=1}^{n_g} \widehat{w}_i\, \mathbf{G}\left(\mathbf{x}_{Qi}\right)\ \left|\mathbf{J}_{ik}^D\right| \tag{25}$$

where n_c is the number of background cells, n_g is the number of Gauss points used in a background cell, $\mathbf{G}$ represents the integrand, Ω_k is the domain of the k^{th} background cell, $\widehat{w}_i$ is the Gauss weighting factor for the i^{th} Gauss point at $\mathbf{x}_{Qi}$, and $\mathbf{J}_{ik}^D$ is the Jacobian matrix for the area integration of the background cell k.

Similarly, we can obtain the formulation of the curve Gauss quadrature as

$$\int_{\Omega} \mathbf{G}\, d\Gamma_t\ = \sum_{l=1}^{n_{ct}} \int_{\Gamma_{tl}} \mathbf{G}\, d\Omega = \sum_{l=1}^{n_{ct}} \sum_{i=1}^{n_{gt}} \widehat{w}_i\, \mathbf{G}\left(\mathbf{x}_{Qi}\right)\ \left|\mathbf{J}_{il}^B\right| \tag{26}$$

n_{ct} is the number of the curve cells that are used to discretize boundary Γ_t, and n_{gt} is number of Gauss points used in a sub-curve, $\mathbf{J}_{il}^B$ is the Jacobian matrix for the curve integration of the sub-boundary l for the Gauss point at $\mathbf{x}_{Qi}$.

B. Nodal integration

In Gauss quadrature a global background cell structure has to be used, this fact made the method not truly meshless. To avoid the use of background cells Beissel and Belytschko [19] have proposed a nodal integration procedure based on a strain smoothing stabilization to eliminate spatial instability in nodal integration. This technique of integration is based on the substitution of the displacement gradient at a node $\mathbf{x}_k$ by averaging the displacement gradient over a cell accompanying that node [20] :

$$\nabla \mathbf{u}^h\left(\mathbf{x}\right) = \int_{\Omega_k} \nabla \mathbf{u}^h\left(\mathbf{x}\right)\ \tilde{W}\left(\mathbf{x}_k - \mathbf{x}\right) d\Omega \tag{27}$$

$\tilde{W}(\mathbf{x}_k - \mathbf{x})$ is a smoothing or weight function associated with $\mathbf{x}_k$, in general we use the following simplest form of the Heaviside-type smoothing function:

$$\tilde{W}\left(\mathbf{x}_k - \mathbf{x}\right) = \begin{cases} 1/A_k & \mathbf{x} \in \Omega_k \\ 0 & \mathbf{x} \notin \Omega_k \end{cases} \tag{28}$$

where A_k is the area of smoothing domain Ω_k. Equation 27 become :

$$\nabla \mathbf{u}^h\left(\mathbf{x}\right) = \frac{1}{A_k} \int_{\Omega_k} \nabla \mathbf{u}^h\left(\mathbf{x}\right)\ d\Omega \tag{29}$$

The surface (or volume) integral can be rewritten by means of the Gauss divergence theorem to a curve (surface) integral :

$$\begin{aligned}\tilde{\nabla} \mathbf{u}^h\left(\mathbf{x}\right) &= \int_{\Gamma_k} \mathbf{u}^h\left(\mathbf{x}\right)\ \mathbf{n}_k\left(\mathbf{x}\right)\ \tilde{W}\left(\mathbf{x}_k - \mathbf{x}\right)\ d\Gamma \\ &= \frac{1}{A_k} \int_{\Gamma_k} \mathbf{u}^h\left(\mathbf{x}\right)\ \mathbf{n}_k\left(\mathbf{x}\right)\ d\Gamma\end{aligned} \tag{30}$$

This nodal integration is based on strain/gradient smoothing technique, this technique is principaly used on the smoothed finite element methods (SFEM) [35] [36][37][38]. Numbers of SFEM models was developped, because of the types of smoothing domains used [43]. Different smoothing domains created based on cells (cell-based S-FEM (CS-FEM)) [40], nodes (node-based S-FEM (NS-FEM)) [42], edges (edge-based S-FEM (ES-FEM)) [41], and faces (face-based S-FEM (FS-FEM)) [40].

V. Error analysis for Radial Point Interpolation Method

Two sources of error are noticed in the case of RPIM: the Radial Basis Function interpolation error and the error in calculation of Galerkin weak form. The first error due to the interpolation can be evaluated by the error in fitting different curves and surfaces. The second error is evaluated through the study of convergence rate of RPIM in case of boundary-value problem.

A. RBF interpolation error

In this section, studies on the accuracy of the RPIM shape functions used for curve fitting are conducted . The fitting of functions is based on the nodal function value sets that are generated at regularly as well as at irregularly distributed nodes. The procedure carried out for curve fitting is : first we create a set of field nodes in the domain where the function is to be fitted, then for a given test node x (usually different from the set of field nodes) where the function is to be fitted, we choose n nodes in the influence domain of x, now we can construct RPIM shape functions, and finaly, using these shape functions we can calculate the function value at x and compare it with the real value.

The interpolation error of curve fitting at point i is measured by :

$$e_t = \frac{1}{n} \sum_{i=1}^{n} \left| \frac{\tilde{f}_i - f_i}{f_i} \right| \tag{31}$$

Table I: Radial Basis Functions with global support used in this study.

RBF	Equation
MQ	$r_i(d_i) = \left({d_i}^2 + (\alpha_c d_c)^2\right)^q$
Exp	$r_i(d_i) = \exp\left[-\alpha_c \left(\frac{d_i}{d_c}\right)^2\right]$
TPS	$r_i(d_i) = d_i^\eta$

where f_i is the true function value at point i and $\tilde{f}_i$ is the fitted function value of the function f at point i in the influence domain.

To construct the RPIM shape function we have to compute the inverse of the matrix **G** (Eq.16), the numerical inversion of this matrix **G** affects the accuracy of interpolation [23], [24]. Therefore, we add a second indicator to the interpolation error wich is the condition number of matrix **G**.

1) Shape parameters analysis: In this section we will see how the shape parameters affect RPIM shape function. Because there is no rule governing the rational choice of the RBF parameters, this theme was and stay a problematic theme when the interpolation by the radial basis functions are used. Several works was made in this axis, we can find the paper of Franke [25] concerning the convergence study of the RBF interpolation, particularly the Multiquadrique (MQ), where he recommends to use an $\alpha_c = 1.25\, d_s/\sqrt{N}$. Hardy [26] recommends the value $\alpha_c = 0.815\ d_s$ where the average influence domain $d_s = (1/N)\sum_{i=1}^{N} d_i$ (d_i is the distance between the i^{th} node and his nearest natural neighbor). Rippa [27] proposes an optimization algorithm for the choice of the rational parameters, which will afterward be improved by Scheuerer [28]. We can also present some recent works including publications of Wang and Liu [29] [30] where they studied the optimal values of RBF-MQ and EXP shape parameters in 2D and 3D [31], they confirm that the condition number of matrix **G** directly affects the accuracy of RBF interpolation. R. Li et al [32] found a range of optimal values of the RBF-MQ shape parameters for the hybrid radial boundary node method.

For this analysis, RPIM shape functions are constructed in a domain of $(x, y) \in [-1,\ 1]\ [-1,\ 1]$ using three sets of $5 \times 5 = 25$ nodes patterns generated within this domain (Fig. 1).

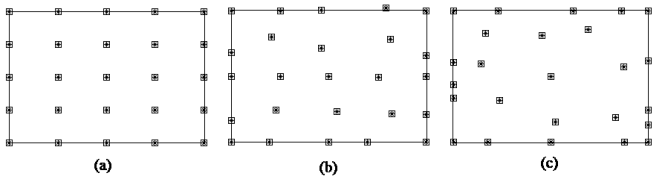

Figure 1: The three sets of nodes patterns.

A total of 100 points are defined as evaluation points. In this study we use three type of RBF with global support: Multiquadric (MQ), Gaussian (EXP), Thin Plate Spline (TPS) (Tab I), in addition of an RBF with compact support (Wu-C2) (Eq.32), with the use of polynomial terms (Eq. 1).

$$r_i(d_i) = \left(1 - \frac{d_i}{\delta_c}\right)^5 \left(8 + 40\frac{d_i}{\delta_c} + 48\frac{{d_i}^2}{\delta_c^2} + 25\frac{{d_i}^3}{\delta_c^3} + 5\frac{{d_i}^4}{\delta_c^4}\right) \tag{32}$$

The evaluation procedure can be prescribe as fellow : for a fixed number of nodes and sampling points, and for a range of RBF shape parameters, we calculate the interpolation error of curve fitting for function defined as :

$$f(x, y) = \sin\left(\sqrt{(x^2 + y^2)}\right) \tag{33}$$

For this exemple we choose a large influence domain that include all nodes of the problem, in order to study only the effect of the choice of the FBR parameters, and once good parameters are selected, we can pass to the choice of dimension of influence domain. All sets of nodes patterns (Fig. 1) are employed in order to evaluate the capacity of RPIM to deal with problems where nodes distribution are irregular.

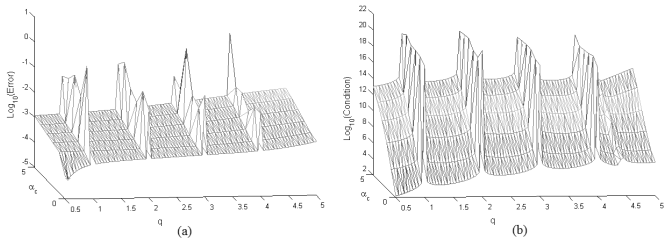

Figure 2: Effect of shape parameters q and α_c of RBF-MQ on (a) Interpolation error and (b) condition number of matrix **G**.

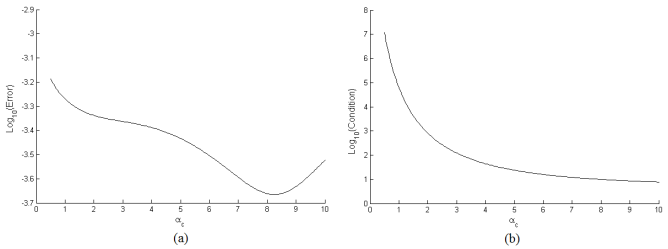

Figure 3: Effect of shape parameter α_c of RBF-EXP on (a) Interpolation error and (b) condition number of matrix **G**.

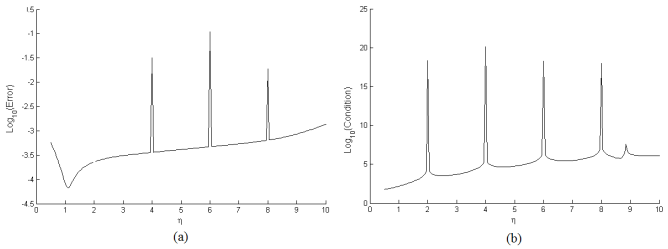

Figure 4: Effect of shape parameter η of RBF-TPS on (a) Interpolation error and (b) condition number of matrix **G**.

Through figures 2 to 9, conclusions can be summarized in the following points:

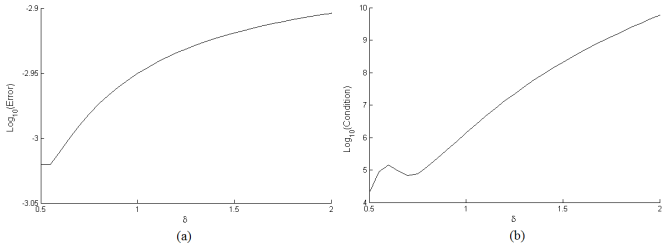

Figure 5: Effect of shape parameter δ of RBF-Wu-C2 on (a) Interpolation error and (b) condition number of matrix **G**.

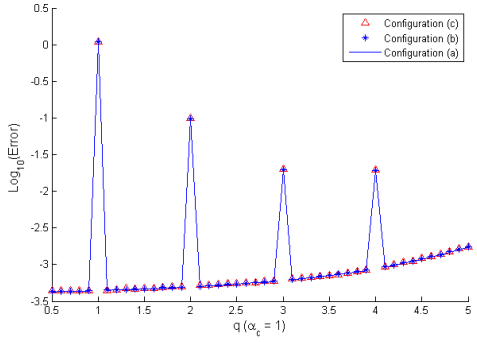

Figure 6: Effect of shape parameter q of RBF-MQ on Interpolation error with different sets of nodes patterns.

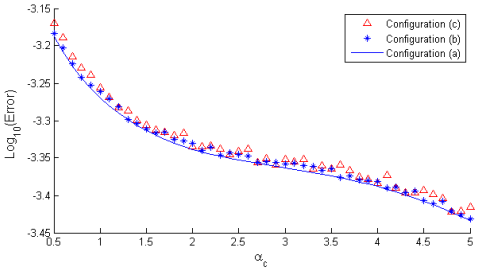

Figure 7: Effect of shape parameter α_c of RBF-EXP on Interpolation error with different sets of nodes patterns.

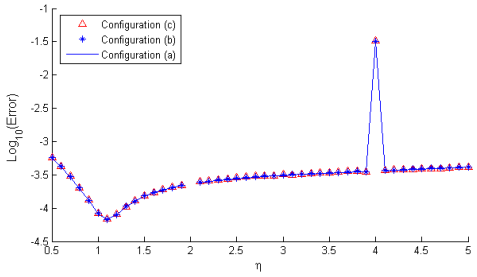

Figure 8: Effect of shape parameter η of RBF-TPS on Interpolation error with different sets of nodes patterns.

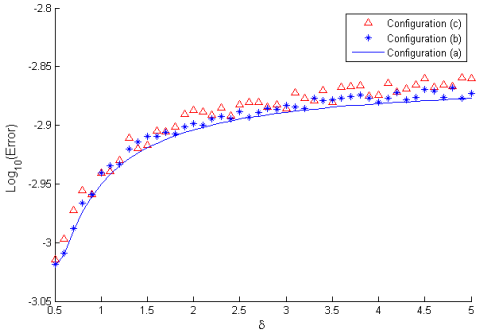

Figure 9: Effect of shape parameter δ of RBF-Wu-C2 on Interpolation error with different sets of nodes patterns.

1) In order to find the good parameters of the FBR, it would be necessary to find the just balance between the error of interpolation and the condition number of matrix **G**.
2) Singular values found on the two basis MQ and TPS are resulting from the bad conditioning of the matrix **G** for these values.
3) Both Gaussian (EXP) and Wu-C2 basic functions present no singular behavior for all shape parameters values.
4) We can notice through figures 6 to 9, that the way nodes are distributed has no significant effect on the quality of RBF interpolation.

2) Dimensions of the influence domain: We suggest now to study the effect of the influence domain size (with circular shape) on the accuracy of RBF interpolation. For this, the domain of the problem is discrétised by 529 nodes distributed in an irrigular manner. By increasing gradually the size of the influence domain, the number of nodes inside thise domain wil increase, then we will proceed to the calculation of the interpolation error and the condition number of matrix **G**.

The obtained results are illustrated in figures (10, 11) when we can draw the following conclusions :

1) The condition number of matrix **G** grows systematically with the increase of the dimensions of the influence domain, thus more the number of nodes inside this domain increases more the matrix **G** will be badly conditioned.
2) The interpolation error does not improve systematically by increasing the number of nodes inside the influence domain, in our opinion, this is due to two factors, the first one is that more the number of nodes implied in the interpolation is important more the number of computational arithmetic operations is important, this engenders numerical calculation errors, the second is that more the number of nodes is important more the condition number of the matrix **G** is larger this means that the matrix is ill-conditioned and its inversion will cause bigger error.
3) Larger influence domain means higher number of nodes included in the interpolation, and it implies the increase on the CPU operations (figure 12). we note that the meshless code is programmed in Matlab and the sim-

ulations are performed on a i5-2.5 GHz computer.

4) From this analysis we recommende that 6 to 25 nodes in the influence domain generate good result and a bigger or smaller number of nodes would lead to larger numerical error.
5) We can mention a technique used in [2] [33] [34], which is based on the concept of the natural neighbor for the construction of the influence domain, the interval recommended by the author for the number of nodes inside (first and second order natural neighbors) Joined what is previously mentioned.

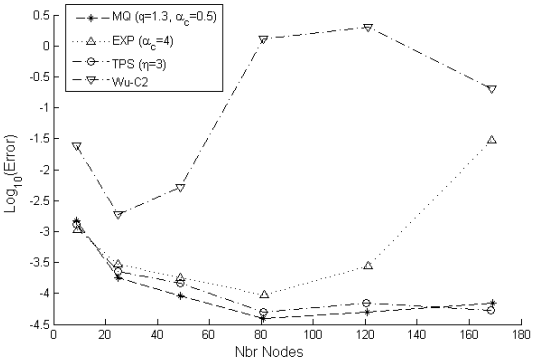

Figure 10: Effect of influence domain dimenssions on Interpolation error with different types of RBF.

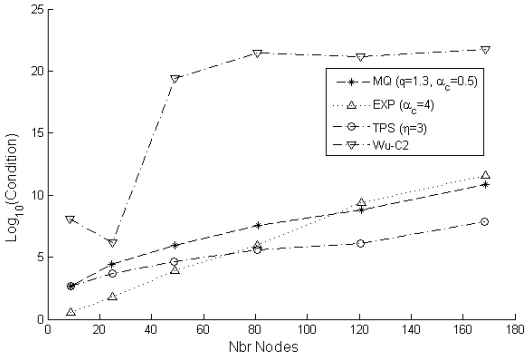

Figure 11: Effect of influence domain dimenssions on condition number of matrix **G** by different types of RBF.

B. Numerical experiments of 2-D solid mechanics problems

1) Error index: The error due to the calculation of Galerkin weak form should be different from that used to evaluate only RBF interpolation over scattered data.

A relative error of displacements is defined as follows :

$$e_{dep} = \frac{\left\| u - \widehat{u} \right\|_{L^2}}{\left\| u \right\|_{L^2}} = \frac{\left(\int\limits_{\Omega} \left(u - \widehat{u} \right)^T \left(u - \widehat{u} \right) \, d\Omega \right)^{1/2}}{\left(\int\limits_{\Omega} (u)^T \, (u) \, d\Omega \right)^{1/2}} \tag{34}$$

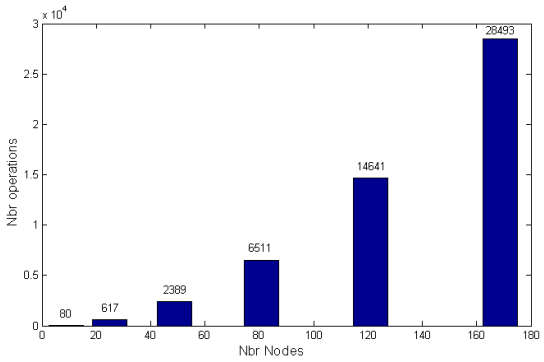

Figure 12: Effect of influence domain dimenssions on the number of computational arithmetic operations.

where $\widehat{u}$ and u are displacements computed by the RPIM and the exact analytical solution, respectively.

The error of energy is defined as follows :

$$e_{Edef} = \frac{\left(\int\limits_{\Omega} \frac{1}{2} \left(\varepsilon - \widehat{\varepsilon} \right)^T c \left(\varepsilon - \widehat{\varepsilon} \right) \, d\Omega \right)^{1/2}}{\left(\int\limits_{\Omega} \frac{1}{2} (\varepsilon)^T \, c \, (\varepsilon) \, d\Omega \right)^{1/2}} \tag{35}$$

Where $\widehat{\varepsilon}$ and ε are strain tensors obtained from the RPIM and the exact analytical closed-form solution, respectively.

In order to evaluate the convergence rates of RPIM methods, it is necessary to define a characteristic length "h". For a grid of triangular T3 background cells:

$$h = \sqrt{\frac{2\, A_\Omega}{N_c}} \tag{36}$$

For a grid of quadrilateral Q4 background cells :

$$h = \sqrt{\frac{A_\Omega}{N_c}} \tag{37}$$

where A_Ω is the area of the problem domain and N_c the number of integration cells.

2) Cantilever beam problem: In this test the accuracy and convergence of combination of shape functions and integration schemes is examined on the problem of a cantilever beam. This problem is widely used to select the optimal parameters of RPIM [29], [30], [31], [32]. Almost all reported conclusions are obtained from this benchmarking numerical experiment.

Consider a cantilever beam shown in Fig.13. The beam is fixed at the left end and subjected to a parabolic traction force at the free end.

The analytical solution is defined as follows [44]:

$$u\,(x,\, y) = -\frac{P y}{6EI} \left[(6L - 3x)\, x + (2 + \upsilon) \left(y^2 - \frac{D^2}{4} \right) \right] \tag{38}$$

$$\upsilon\,(x,\, y) = \frac{P}{6EI} \left[3\,\upsilon\, y^2\, (L - x) + (4 + 5\,\upsilon)\, \frac{D^2 x}{4} + (3L - x)\, x^2 \right] \tag{39}$$

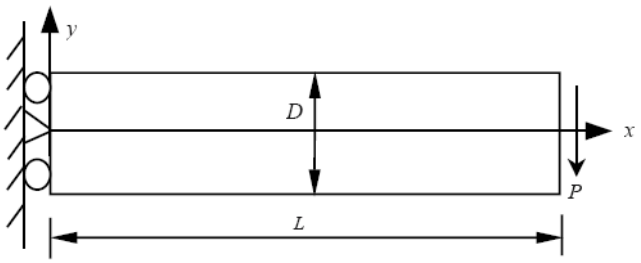

Figure 13: Cantilever beam problem.

where the moment of inertia I of the beam is given by $I = \frac{D^3}{12}$.

The corresponding stresses are :

$$\sigma_{xx}(x, y) = -\frac{P(L-x)y}{I} \tag{40}$$

$$\sigma_{yy} = 0 \tag{41}$$

$$\tau_{xy}(x, y) = \frac{P}{2I}\left[\frac{D^2}{4} - y^2\right] \tag{42}$$

The beam parameters are taken as $P = -1000N$, $E = 3 \times 10^7 MPa$, $\upsilon = 0.3$, $D = 12mm$, $L = 48mm$.

3) Shape parameters analysis: For this test, two configurations of nodes will be used: 325 nodes distributed in a regular and irregular way respectively 14. Only two radial basis functions will be handled: the multiquadric (MQ) and the Gaussienne (EXP). Here circular influence domain circumvents 8 to16 nodes is used for each Gaussian point. Polynomial term is included for the rbf interpolation. For the gauss integration we use $4 \times 4 = 16$ gauss points for each cell of the set of 288 (24×12) background cells (figure 15). First, we study the effect of the Multiquadric shape parameters (MQ), results will be illustrated in figures 16, 17.

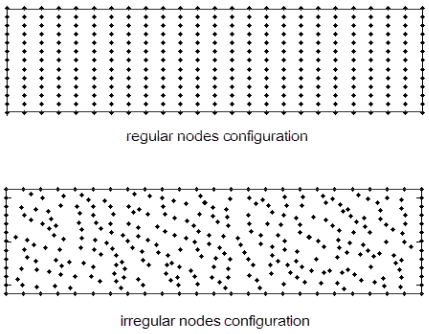

Figure 14: Nodes configurations of the cantilever beam problem.

1) For a uniform distribution of nodes, the optimal error values are registered for q between $1.5 - 2$ and all mentioned α_c ($\alpha_c = 0.5, 1, 1.5, 2$, we avoided the value of $q = 2$ because it is the particular value which makes the matrix $\mathbf{G}$ singular or strongly ill-conditioned.
2) For an irregular nodes distribution, the optimal value of q varies according to the value of α_c.

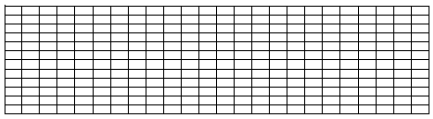

Figure 15: (24×12) background cells for numerical integration.

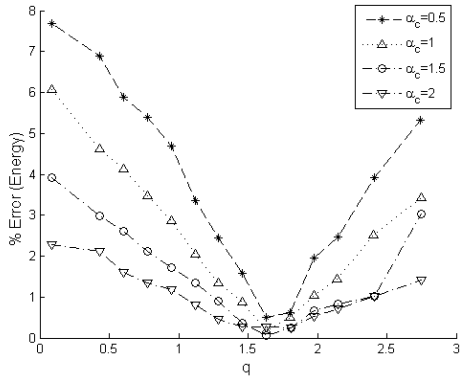

Figure 16: Effect of RBF-MQ shape parameters on energy error for regular nodes distribution.

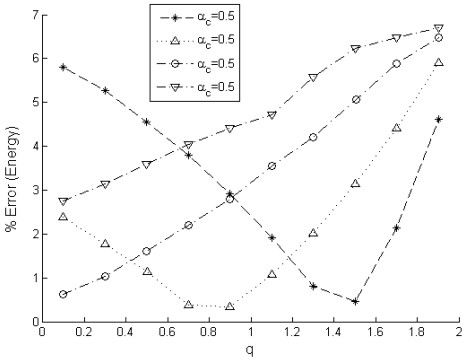

Figure 17: Effect of RBF-MQ shape parameters on energy error for irregular nodes distribution.

3) The recommended values for the Multiquadric (MQ) are: $\alpha_c = 0.5 \sim 2$ and $q = 0.4 \sim 2.2$ with the exception of the singular values (integers).

Secondly, we study the effect of the Gaussian shape parameters (EXP), results will be illustrated in figures 18.

1) For a uniform node disctribution, the values of the energy error remain relatively invariant for $\alpha_c > 0.03$.
2) For an irregular nodes distribution, the behavior of the error according to α_c is almost the same that for the uniform configuration.
3) The recommended values for Gaussian (EXP) are : $\alpha_c = 0.2 \sim 1$.

4) Dimensions of the influence domain: In this analysis, we adopt a configuration of 975 (39x25) nodes uniformly distributed, the same configuration is used for quadrilateral background cells (figure 19), four configurations of shape parameters for the FBR will be used : RBF-MQ with: $q = 1.3$

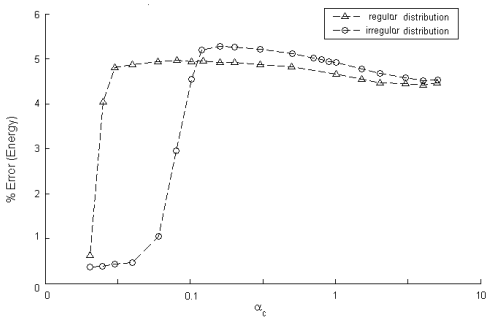

Figure 18: Effect of RBF-EXP shape parameters on energy error for regular/irregular nodes distribution.

and $\alpha_c = 0.5$ and $q = 1.9$ and $\alpha_c = 1.5$, RBF-EXP with: $\alpha_c = 0.2$ and $\alpha_c = 0.6$. The number of Gauss points is maintained to 16 points by cell.

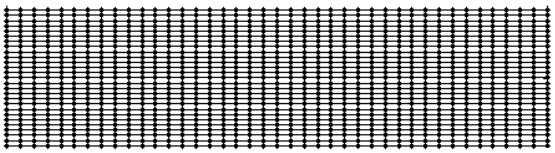

Figure 19: The two combined configurations of 975 (39x25) nodes and 1040 (40x26) background cells.

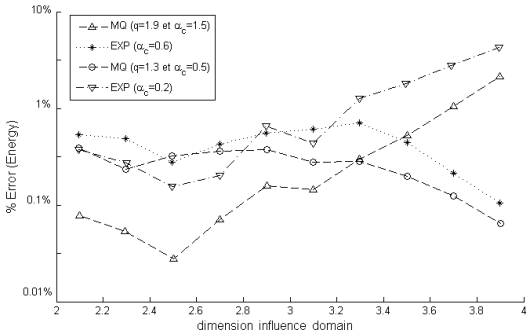

Figure 20: Effect of influence domain dimenssions on energy error.

1) Large size of influence domain does not imply systematically a good precision, quite the opposite, number of arithmetic operations required for the calculation increase, what would have consequence on increasing the CPU time (figure 21).
2) The number of nodes recommended to reach a good quality is of $9 \sim 30$ nodes inside the influence domain.

5) Number of Gauss points: To analyze how the number of Gauss points by cell used on the Gauss integration technique affect the accuracy of RPIM, we have to fix these parameters : for nodal discretization and background cells we use the previous uniform configurations Fig.14 and 15, two radial basis functions are considered : the RBF-MQ with $q = 1.9$

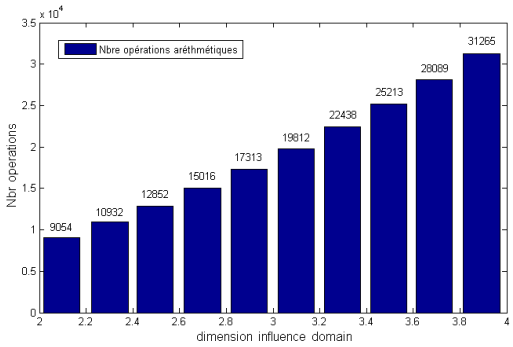

Figure 21: Effect of influence domain dimenssions on the number of computational arithmetic operations.

and $\alpha_c = 1.5$, the RBF-EXP with $\alpha_c = 0.2$, the influence domain being determined by 6-12 nodes inside.

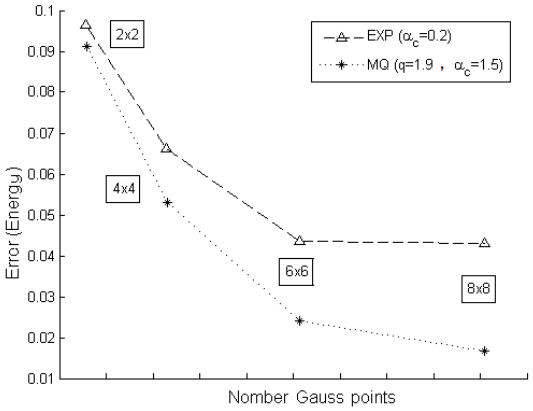

Figure 22: Energy error in function of the number of Gauss points.

Figure 22 shows the variation of the energy error according to the number of Gauss points of by cell, we notice that more the number of gauss points will be important, more the quality of RPIM results will be better until a relative stabilization for a number bigger than $64 = 8 \times 8$ quadrature points. On the other hand, it would be necessary to pay attention to the CPU time for numerical calculations which will tend to increase proportionally with the increase of Gauss points used. We can recommend to take a 4×4 up to 6×6 Gauss points for rectangular cells.

6) Effect of the integration technique: The objective of this section is the study of two numerical integration techniques : the classical Gauss integration and the Stabilized conforming nodal integration (SCNI).

In all what follows, the Radial basic function chosen is the Gaussian (EXP) with $\alpha_c = 0.2$, with addition of 1^{st} order polynomial terms, influence domain being determined with 8-16 nodes inside. A total of 6×6 Gauss points are used for the classic Gauss quadrature.

five set of regularely distributed nodes pattern and in the same time integration cells are used for this exemple : 1150, 798, 520, 360, 284.

We notice, first, that the convergence rates of meshfree methods (RPIM, SRPIM) are better than those obtained by the FEM, this is due to the higher order of RBF interpolation comparing with the linear interpolation used in FEM triangular element, secondly, among RPIM meshfree methods the one who presents a better rate of convergence is SRPIM, who possesses the advantage of using a nodal stabilized integration with regard to the classic RPIM which use Gauss integration.

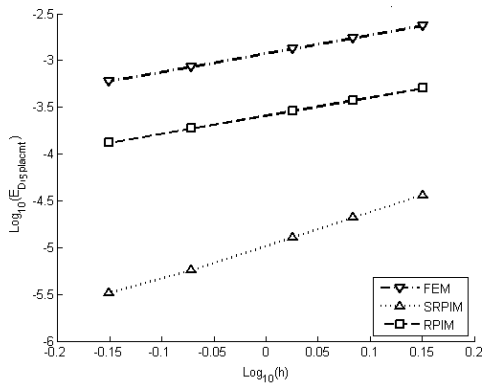

Figure 23: Relative error in displacement calculated for FEM, RPIM, SRPIM.

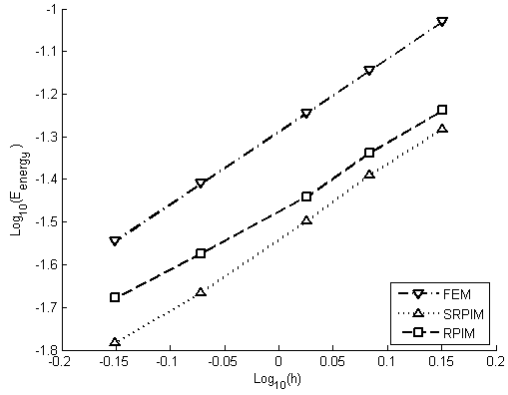

Figure 24: Relative energy error calculated for FEM, RPIM and SRPIM.

C. *Infinite plate with a circular hole*

We consider here a plate with a central circular hole with raduis $a = 1m$ subjected to a unidirectional tensile load of $F = 1N/m$ in the x-direction, due to symmetry, only the upper right quadrant of the plate is modelled as shown in Figure 25. Symmetry conditions are imposed on the left and bottom edges. The inner boundary is traction free. Plane strain conditions are assumed, and the problem constants are : $L = 5m, a = 1m, E = 10^3 N/m^2, \nu = 0,3, P = 1N/m$. analytical solution of these problem [44]:

$$u_1 = \frac{a}{8\mu}\left[\frac{r}{a}(\kappa+1)\cos\theta + 2\frac{a}{r}((1+\kappa)\cos\theta+\cos 3\theta) - 2\frac{a^3}{r^3}\cos 3\theta\right] \quad (43)$$

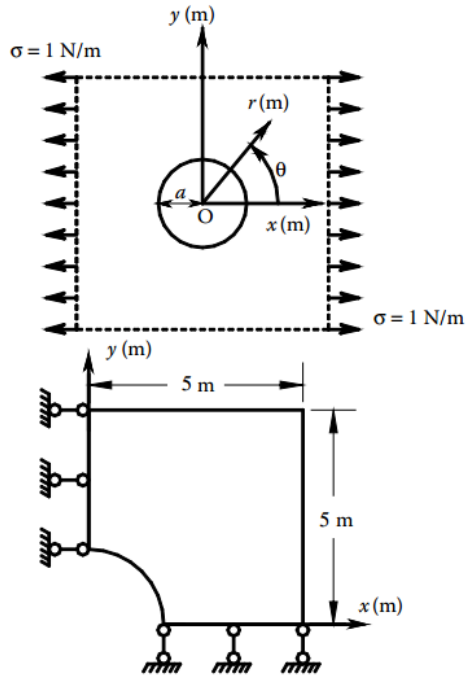

Figure 25: Geometry of the infinite plate with a hole problem.

$$u_2 = \frac{a}{8\mu}\left[\frac{r}{a}(\kappa-3)\sin\theta + 2\frac{a}{r}((1-\kappa)\sin\theta+\sin 3\theta) - 2\frac{a^3}{r^3}\sin 3\theta\right] \quad (44)$$

where (r, θ) are the polar coordinates with θ measured counter-clockwise from the positive x axis, $\mu = E/(2(1+\nu))$ et $\kappa = 3 - 4\nu$.

The analytical solution for the stresses of an infinite plate is :

$$\sigma_x(x, y) = 1 - \frac{a^2}{r^2}\left\{\frac{3}{2}\cos 2\theta + \cos 4\theta\right\} + \frac{3a^4}{2r^4}\cos 4\theta \quad (45)$$

$$\sigma_y(x, y) = -\frac{a^2}{r^2}\left\{\frac{1}{2}\cos 2\theta - \cos 4\theta\right\} - \frac{3a^4}{2r^4}\cos 4\theta \quad (46)$$

$$\sigma_{xy}(x, y) = -\frac{a^2}{r^2}\left\{\frac{1}{2}\sin 2\theta - \sin 4\theta\right\} + \frac{3a^4}{2r^4}\sin 4\theta \quad (47)$$

The displacement boundaryconditions are given by :

on the edge of $x = 0$: $u_x = 0$, on the edge of $y = 0$: $u_y = 0$.

As in the previous example, five nodes configurations will be used for this problem also, the total number of nodes used is: 169, 289, 625, on 1089 and 1681. Figures 26, 27, illustrate convergence rates of results obtained from RPIM, SRPIM and FEM. We notice as well in this problem that the convergence rates obtained from meshless methods, are better than those obtained by the FEM, and among the RPIM methods, SRPIM presents a better precision in term of displacement error and in energy error, what confirms the quality of the SCNI integration.

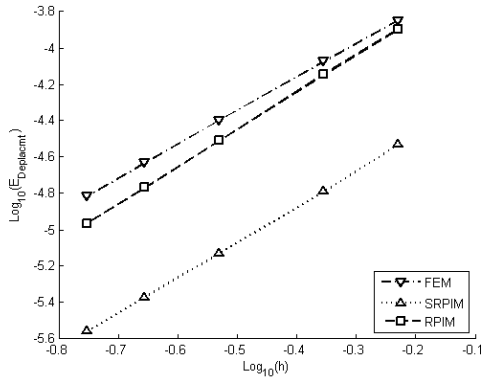

Figure 26: Relative error in displacement calculated for FEM, RPIM, SRPIM.

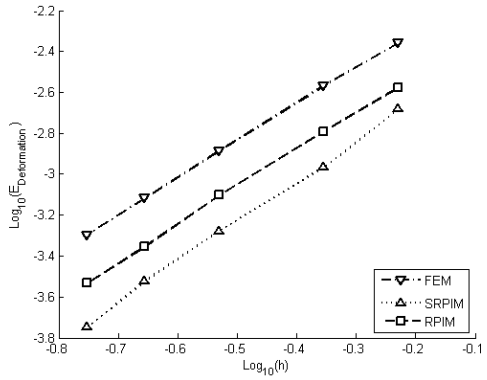

Figure 27: Relative energy error calculated for FEM, RPIM and SRPIM.

D. Distortion analysis

The example treated in this test is similar to the precedent test of cantilever beam (Figure 13), but with a different geometry and load (Figure 28), this geometry will be discretised by various nodes configurations (Figure 29).

The Radial basic function chosen is the Gaussian (EXP) with $\alpha_c = 0.2$, influence domain being determined with 8-16 nodes inside. A total of 6×6 Gauss points are used for the classic Gauss quadrature.

The exact solution calculated on the field of stress :

$$\sigma_{xx}(x) = \frac{3}{2} y, \quad \sigma_{yy}(x) = 0, \quad \sigma_{xy}(x) = 0 \tag{48}$$

The exact solution calculated on the field of strain :

$$\begin{aligned} \varepsilon_{xx}(x) &= \frac{3E(1-\upsilon)}{2(1-\upsilon)(1-2\upsilon)} y, \quad \varepsilon_{yy}(x) \\ &= \frac{3E\upsilon}{2(1-\upsilon)(1-2\upsilon)} y, \quad \varepsilon_{xy}(x) \\ &= 0 \end{aligned} \tag{49}$$

We notice in Figures 30 and 31 that for the first nodes configuration distributed in a regular way (configuration (1)), all RPIM methods gives satisfactory results and better than those obtained by finite element method (with linear triangular element mesh).

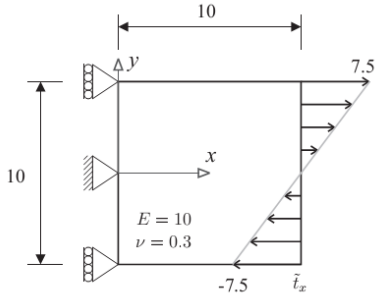

Figure 28: Model to examine distortional effects.

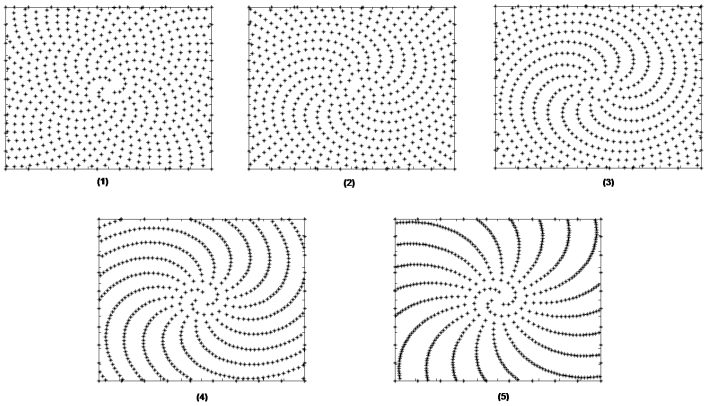

Figure 29: Grids used to examine the influence of distortion.

For the last nodes configuration, the most severe twisted configuration, and in spite of the fact that we use an influence domain guaranteeing a minimum number of nodes inside the latter, we notice that all RPIM methods diverges but by different degrees, the method which seems the least affected by this distortion is the S-RPIM (with SCNI technique). In summary, the more the distortion of the meshing of nodes is big, the more the error in displacement and in energy increases, however the methods using the SCNI integration technique are less affected by this degradation than those using the classical Gauss integration.

VI. Conclusion

In this paper a numerical analysis was performed on the RPIM meshless method with two integration schemes. The performance in the RBF shape function and in linear elasticity. It was shown that the Radial basis interpolation was important to the global accuracy of the RPIM. It was found that the condition number of the matrix **G** heavily affects the accuracy of interpolation. Shape parameters also had important effects on the condition number. A range of good shape parameters should balance the accuracy and the condition number. The folowing notes can be retained : Error was large when shape parameters takes singular values (q = integer values for RBF-MQ). Through numerical experiments, a range of shape parameters was found. Parameters from this range can give

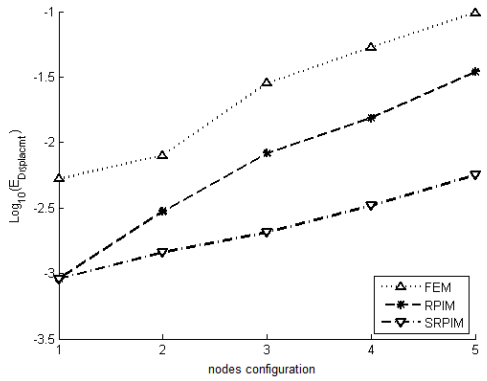

Figure 30: Relative error of displacement on results obtained by FEM, RPIM and SRPIM with several nodes configurations.

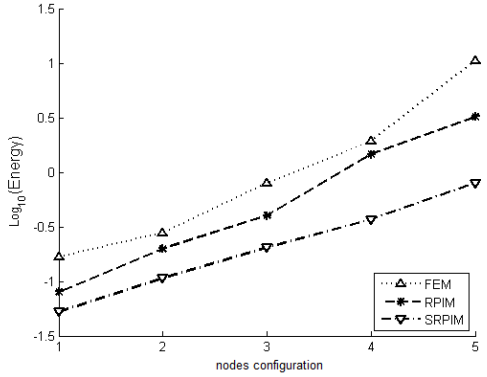

Figure 31: Energy error on results obtained by FEM, RPIM and SRPIM with several nodes configurations.

relatively good results. For regular nodal distribution, when the number of nodes inside the influence domain ranges from 6 to 25, the accuracy was high. With adding polynomial term and an appropriate influence domain size, shape parameters can be chosen from a larger range of values avoiding singular ones. Nodal distribution had little effect on the accuracy of RPIM interpolation. Further more it was observed that the SCNI integration scheme was less sensitive to distortion than the Gaussian integration scheme, and gives excellent results when compared to a Gaussian integration rule.

REFERENCES

[1] N. S. Lee, , K.J. Bathe , Effects of element distortions on the performance of isoparametric elements. Int. J. Numer. Meth. Engng., 36, 3553-3576 (1993).

[2] E. Cueto, N. Sukumar, B. Calvo, M. A. Martínez, J. Cegoñino, M. Doblaré, Overview and recent advances in natural neighbour galerkin methods, Archives of Computational Methods in Engineering, Volume 10, Issue 4, 307-384 (2003).

[3] J. Slater, Electronic energy bands in metals, Phys. Rev. 45, 794-801 (1934).

[4] R. Frazer, W. Jones, S. Skan, Approximations to functions and to the solutions of differential equations, Great Britain Aero Counc. London. Rep. and Memo. No.1799 1, 517-549 (1937).

[5] C. Lanczos, Trigonometric interpolation of empirical and analytical functions, J. Math. Phys 17, 123-199 (1938).

[6] M. B. Liu, G. R. Liu, Smoothed Particle Hydrodynamics (SPH): an Overview and Recent Developments, Archives of Computational Methods in Engineering, Volume 17, Issue 1, pp 25-76 (2010).

[7] L. Lucy, A numerical approach to testing the ssion hypothesis, Astron. J. 82, 1013-1024 (1977).

[8] B. Nayroles, G. Touzot, P. Villon, Generalizing the finite element method: diffuse approximation and diffuse elements, Computational Mechanics, 10 (5), 307-318 (1992).

[9] W. K. Liu, S. Jun, Y. F. Zhang, Reproducing kernel particle methods, Int. J. Numer. Methods Eng. 20 (8-9), 1081-1106 (1995).

[10] W. K. Liu, Y. Chen, S. Jun, J. S. Chen, T. Belytschko, C. Pan, R. A. Uras, C. T. Chang, Overview and applications of the reproducing Kernel Particle methods, Archives of Computational Methods in Engineering, Volume 3, Issue 1, pp 3-80 (1996).

[11] Y. Lu, T. Belytschko, L. Gu, A new implementation of the element free galerkin method, Computer Methods in Applied Mechanics and Engineering 113 (3-4), 397-414 (1994).

[12] J. G. Wang, G. R. Liu, Radial point interpolation method for elasto-plastic problems, Proc. of the 1st Int. Conf. On Structural Stability and Dynamics, 703-708 (2000).

[13] S. N. Atluri, T. Zhu, A new meshless local petrov-galerkin (mlpg) approach in computational mechanics, Computational Mechanics 22 (2), 117-127 (1998).

[14] T. Belytschko, Y. Lu, L. Gu, Element-free galerkin methods, Int. J. Numer. Methods Eng. 37 (2), 229-256 (1994).

[15] J. Dolbow, T. Belytschko, An introduction to programming the meshless Element F reeGalerkin method, Archives of Computational Methods in Engineering, Volume 5, Issue 3, pp 207-241 (1998).

[16] G. Liu, Y. Gu, A point interpolation method, 4th Asia-Pacific Conference on Computational Mechanics Singapore, 1009-1014 (1999).

[17] G. R. Liu, Y. T. Gu, A point interpolation method for two-dimensional solids, Int. J. Num. Meth. Eng. 50, 937-951 (2001).

[18] G. Liu, Y. Gu, A matrix triangularization algorithm for the polynomial point interpolation method, Computer Methods in Applied Mechanics and Engineering 192 (19), 2269-2295 (2003).

[19] S. Beissel, T. Belytschko, Nodal integration of the element-free galerkin method, Computer Methods in Applied Mechanics and Engineer-ing 139, 49-74 (1996).

[20] J. Chen, C. Wu, S. Yoon, Y. You, A stabilized conform-ing nodal integration for galerkin mesh-free methods, Int. J. Num. Meth. Eng. 50, 435-466 (2001).

[21] . J. Chen, S. Yoon, C. Wu, Non-linear version of stabilized conforming nodal integration for galerkin mesh-free methods, Int. J. Num. Meth. Eng. 53, 2587-2615 (1993).

[22] M. Golberg, C. Chen, H. Bowman, Some recent results and proposals for the use of radial basis functions in the bem, Engineering Analysis with Boundary Elements 23, 285-296 (1999).

[23] J. Boyd, K. Gildersleeve, Numerical experiments on the condition number of the interpolation matrices for radial basis functions, Applied Numerical Mathematics 61 (4), 443-459 (2011).

[24] J. Chen, W. Hu, H. Hu, Localized radial basis function with partition of unity properties, Progress on Meshless Methods Computational Methods in Applied Sciences 11, 37-56 (2009).

[25] R. Franke, Scattered data interpolation: Tests of some methods, Mathematics of Computation 38(157), 200-292 (1982).

[26] R. Hardy, Multiquadric equations of topography and other irregular surfaces, Journal of Geophysical Research 176, 1905-1915 (1971).

[27] S. Rippa, An algorithm for selecting a good value for the parameter c in ra-dial basis function interpolation, Advances in Computational Mathematics 11, 193-210 (1999).

[28] M. Scheuerer, An alternative procedure for selecting a good value for the parameter c in rbf-interpolation, Advances in Computational Mathematics 34, 105-126 (2011).

[29] J. Wang, G. Liu, A point interpolation meshless method based on radial basis functions, International Journal for Numerical Methods in Engineering, 54 (11), 1623-1648 (2002).

[30] J. Wang, G. Liu, On the optimal shape parameters of radial basis func-tions used for 2d meshless methods, Computer Methods in Applied Mechanics and Engineering 191 (23/24), 2611-2630 (2002).

[31] G. Liu, G. Zhang, Y. GU, J. W. and, A meshfree radial point interpolation method (rpim) for three dimensional solids, Computational Mechanics, 36 (6), 421-430 (2005).

[32] L. Li, J. Zhu, S. Zhang, A hybrid radial boundary node method based on radial basis point interpolation, Engineering Analysis with Boundary Elements, 33 (11), 1273-1283 (2009).

[33] L. Dinis, R. N. Jorge, J. Belinha, Analysis of 3d solids using the natural neighbour radial point interpolation method, Computer Methods in Applied Mechanics and Engineering 196 (13-16), 2009-2028 (2007).

[34] L. Dinis, R.N. Jorge , J. Belinha, Analysis of plates and laminates using the natural neighbour radial point interpolation method, Engineering Analysis with Boundary Elements, Volume 32, Issue 3, Pages 267-279 (2008).
[35] G.R. Liu, K.Y. Dai, T.T. Nguyen, A smoothed finite element method for mechanics problems, Comput. Mech. 39, 859-877 (2007).
[36] K.Y. Dai, G.R. Liu, Free and forced vibration analysis using the smoothed finite element method (SFEM), J. Sound Vib. 301, 803-820 (2007).
[37] G.R. Liu, T.T. Nguyen, K.Y. Dai, K.Y. Lam, Theoretical aspects of the smoothed finite element method (SFEM), Int. J. Numer. Methods Eng.71 (8), 902-930, (2007).
[38] G.R.Liu, A generalized gradient smoothing technique and the smoothed bilinear form for Galerkin formulation of a wide class of computational methods, International Journal of Computational Methods, 5 (2), 199-236 (2008).
[39] G.R. Liu , Thoi. T. Nguyen, K.Y. Lam, An edge-based smoothed finite element method (ES-FEM) for static, free and forced vibration analysis.Journal of Sound and Vibration; 320: 1100-1130 (2009).
[40] Thoi. T. Nguyen, G.R. Liu , K.Y. Lam, G. Y. Zhang, A face-based smoothed finite element method (FS-FEM) for 3D linear and nonlinear solid mechanics problems using 4-node tetrahedral elements. International Journal for Numerical Methods in Engineering; 78: 324-353 (2009).
[41] Z. C. He , G.R. Liu , Z.H. Zhong , S.C. Wu , G.Y. Zhang , and A. G. Cheng, An edge-based smoothed finite element method (ES-FEM) for analyzing three-dimensional acoustic problems.Computer Methods in Applied Mechanics and Engineering; 199: 20-33 (2009).
[42] G.R. Liu, T. Nguyen-Thoi, H. Nguyen-Xuan, K.Y. Lam, A node-based smoothed finite element method (NS-FEM) for upper bound solutions to solid mechanics problems, Computers and Structures, 87 (1–2), 14-26 (2009).
[43] G. R. Liu, N. T. Trung, Smoothed Finite Element Method, Taylor and Francis, CRC Press (2010).
[44] S. Timoshenko, J. Goodier, Theory of Elasticity, McGraw-Hill, New York, (1970).
[45] G. Liu, Meshfree methods: moving beyond the finite element method, 2nd ed. Boca Raton: Taylor and Francis, CRC Press (2002).